RESEARCH ARTICLE

A Holistic Solution to Icing by Acoustic Waves: De-Icing, Active Anti-Icing, Sensing with Piezoelectric Crystals, and Synergy with Thin Film Passive Anti-Icing Solutions

Jaime del Moral, Laura Montes, Victor Joaquin Rico-Gavira, Carmen López-Santos, Stefan Jacob,* Manuel Oliva-Ramirez, Jorge Gil-Rostra, Armaghan Fakhfouri, Shilpi Pandey, Miguel Gonzalez del Val, Julio Mora, Paloma García-Gallego, Pablo Francisco Ibáñez-Ibáñez, Miguel Angel Rodríguez-Valverde, Andreas Winkler, Ana Borrás,* and Agustin Rodriguez González-Elipe*

Icing has become a hot topic both in academia and in the industry given its implications in transport, wind turbines, photovoltaics, and telecommunications. Recently proposed de-icing solutions involving the propagation of acoustic waves (AWs) at suitable substrates may open the path for a sustainable alternative to standard de-icing or anti-icing procedures. Herein, the fundamental interactions are unraveled that contribute to the de-icing and/or hinder the icing on AW-activated substrates. The response toward icing of a reliable model system consisting of a piezoelectric plate activated by extended electrodes is characterized at a laboratory scale and in an icing wind tunnel under realistic conditions. Experiments show that surface modification with anti-icing functionalities provides a synergistic response when activated with AWs. A thoughtful analysis of the resonance frequency dependence on experimental variables such as temperature, ice formation, or wind velocity demonstrates the application of AW devices for real-time monitoring of icing processes.

1. Introduction

Icing on surfaces is a common event hindering the development of both domestic and industrial activities and processes. Icing can be quite deleterious, provoking accidents (e.g., in aviation or autonomous driving), or the malfunction of industrial and energy production facilities (e.g., wind turbines, marine structures, heat exchangers, and telecommunication antennas). Icing may also impact daily used instruments or vehicles (e.g., displays, outdoor sensors, cameras, and windscreens in cars, among others). Therefore, a large variety of procedures have been developed and applied during the last years trying to mitigate the effect of icing in a large variety of scenarios. These can be classified into three main

J. del Moral, L. Montes, V. J. Rico-Gavira, C. López-Santos,
M. Oliva-Ramirez, J. Gil-Rostra, A. Borrás, A. R. González-Elipe
Nanotechnology on Surfaces and Plasma Lab
Materials Science Institute of Seville (CSIC-US)
c/ Américo Vespucio 49, Seville 41092, Spain
E-mail: anaisabel.borras@icmse.csic.es; arge@icmse.csic.es
C. López-Santos
Departamento de Física Aplicada I, Escuela Politécnica Superior
Universidad de Sevilla
C/ Virgen de Africa 7, Seville 41011, Spain

The ORCID identification number(s) for the author(s) of this article can be found under https://doi.org/10.1002/adfm.202209421.

© 2023 The Authors. Advanced Functional Materials published by Wiley-VCH GmbH. This is an open access article under the terms of the Creative Commons Attribution-NonCommercial-NoDerivs License, which permits use and distribution in any medium, provided the original work is properly cited, the use is non-commercial and no modifications or adaptations are made.

DOI: 10.1002/adfm.202209421

S. Jacob, A. Fakhfouri, S. Pandey, A. Winkler
Leibniz IFW Dresden
SAWLab Saxony
Helmholtzstr. 20, 01069 Dresden, Germany
E-mail: stefan.jacob@ptb.de
M. Oliva-Ramirez
Departamento de Física Atómica
Molecular y Nuclear
Avd. Reina Mercedes s/n, Seville 41012, Spain
M. Gonzalez del Val, J. Mora, P. García-Gallego
National Institute for Aerospace Technology (INTA)
Ctra. Ajalvir km. 4, Torrejón de Ardoz 28850, Spain
P. F. Ibáñez-Ibáñez, M. A. Rodríguez-Valverde
Departamento de Física Aplicada
Universidad de Granada
Avd. de Fuente Nueva s/n, Granada 18002, Spain

groups, namely, anti-icing (to avoid the formation of ice by applying surface engineering methods), de-icing (to remove ice once it is accreted on a surface), and combined anti-icing and de-icing. De-icing relies on various physical principles, including the application of low-temperature freezing liquids,[1] the use of the Joule effect,[2,3] solar actuation and photothermal effects,[4–6] the de-icing activation with plasmas,[7] the implementation of plasmonic nanoparticles,[8] the application of bulk or guided ultrasonic sound waves in the kHz range generated by external piezoelectric devices,[9,10] or, as reported very recently, the use of surface acoustic waves (SAWs) with suitable substrates coated with a piezoelectric thin film.[11]

In this article, we go a step forward and disclose a series of basic ice-substrate interactions upon activation with bulk acoustic waves (AWs) generated in excited piezoelectric substrates. Thus, unlike previous works using piezoelectric actuators outside the icing area to generate propagating ultrasounds (kHz range) for de-icing,[9,10] we propose a radically different approach relying on the generation of AWs (MHz range) on piezoelectric substrates where ice is formed. This approach involves the direct interaction of the generated AWs with ice. The investigation follows a holistic approach and studies de-icing processes of ice accumulated on surfaces, the promotion of an anti-icing function preventing the formation of ice (i.e., active anti-icing), the reduction of ice adhesion, and, interestingly, the possibilities to implement the proposed device as a smart sensor-actuator system (see **Scheme 1**). In general, AWs can be generated by the electrical activation of piezoelectric materials through the inverse piezoelectric effect.[12] This can give rise, for example, to bulk or plate AWs, affecting in this case the whole structure and thickness of the material, or be confined to the surface, as for the so-called surface acoustic waves (SAWs).[13–15]

Although as mentioned above, the application of external piezoelectric devices to generate ultrasounds onto a variety of materials has been claimed since some time ago as a suitable technological procedure to activate de-icing processes or to prevent the formation of ice on surfaces,[9,10,16] only recently it has been proposed the use of SAWs for small agglomerates de-icing[11] and/or for ice detection.[17–19] Such an innovative approach is in its infancy and still full of open questions and challenges to address. Thus, as the next step toward the development of a viable technology, it is essential to demon-

strate a robust experimental scheme that implies full control over critical aspects such as the de-icing capacity outside the area defined by the electrodes (i.e., to discard possible Joule effects),[11] the demonstration that AW de-icing can be used not only in the laboratory for small ice agglomerates but in real or close to real environmental conditions and large amounts of ice, or the possibility that AWs can be used for both sensing and actuation. Besides approaching the problem for the first time from such a global perspective, we propose herein to advance into the combination of active and passive functionalities in the same device and exploit possible synergies arising from the incorporation of anti-icing thin films onto the piezoelectric substrates. More specifically, we address these issues to gain empirical knowledge about the effects of AWs on accreted ice, ice formation on activated surfaces, and the operational possibilities of AW devices under realistic environmental conditions in an icing wind tunnel (IWT). Both de-icing of already formed ice and active anti-icing experiments (i.e., avoiding the formation of ice on continuously activated substrates) have been performed with $LiNbO_3$ piezoelectric plates. The selection of $LiNbO_3$ plates as model system for this investigation has been dictated by the need of thoroughly controlling basic physical features such as the propagation and characteristics of the AWs, to have a well-defined set of conditions for simulation, and to ensure that Joule effects associated to the electrodes are negligible. Specifically, shear modes of standing Lamb waves[20] were generated by applying an activation signal in the range of a few MHz and employing two planar electrodes rather than interdigitated electrodes (IDTs) as for SAWs.[11,13–15] Such a configuration is simpler for manufacturing, reduces spurious heating effects associated with the electrodes, is compatible with piezoelectric polymers and permits the realization of different experiments such as ice adhesion, ice accretion or ice melting with the same device. A variable that has also been explored in this work is the effect of modifying the surface state of $LiNbO_3$ with anti-icing coatings and multilayers. We designate as passive anti-icing the function of some surface terminations preventing the formation of ice or repelling its accretion,[21–23] for example, by hydrophobic and superhydrophobic surface functionalization (although superhydrophobicity is not synonymous of an effective anti-icing function).[24,25] Herein, the modification of the surface state of $LiNbO_3$ has been carried out with a double perspective: on the one hand to make
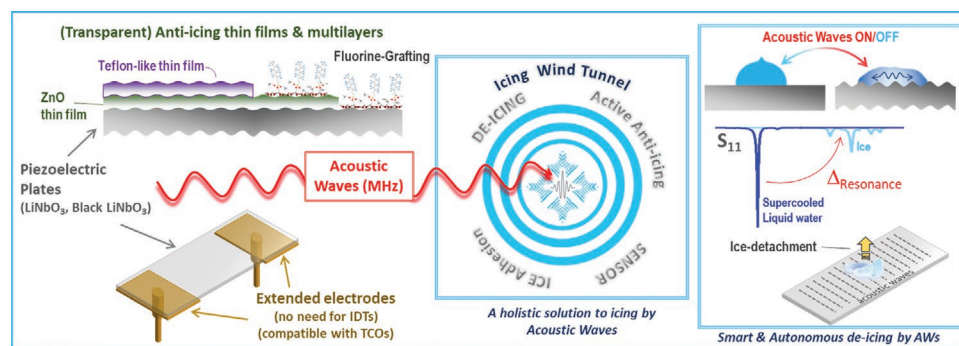
Scheme 1. Schematic representation of the scope of this article, from the application of model piezoelectric plates and anti-icing thin films and multilayers (left), which going through a holistic approach to ice-phobic solutions (middle) settles the path to the development of smart and autonomous de-icing systems incorporating both sensing and actuation (right).

its surface hydrophobic (LiNbO$_3$ surface is hydrophilic) and, on the other, to prove whether the AW activation of the coated substrate remains effective to induce de-icing (i.e., to demonstrate whether AW attenuation effects are negligible when a passive anti-icing layer is deposited onto the piezoelectric substrate material). For this purpose, we have deposited onto the LiNbO$_3$ a ZnO thin film some hundreds of nanometers thick, which is further modified following two different strategies: first by plasma deposition of a CF$_x$ thin film (i.e., Teflon-like layer)[26,27] known for its hydrophobic and passive anti-icing properties and, second, by molecular grafting of a perfluorooctyltriethoxysilane (PFOTES) molecule, a surface termination that induces hydrophobicity and anti-icing surface responses.[28,29] ZnO is a typical piezoelectric material that, in the form of relatively thick films (generally over 5 µm), is widely used to generate SAWs with IDTs for a large variety of applications.[24,30,31] Finally, some comparative experiments have also been carried out with black LiNbO$_3$, a partially reduced variety of piezoelectric material showing piezoelectric but not pyroelectric activity.[32] Discarding pyroelectric effects during de-icing and therefore sustaining the use of fully transparent LiNbO$_3$ plates (in the future other transparent piezoelectric materials or layers as well) and low thermal conductive materials for AW activation should widen the application of this technology beyond de-icing on aluminium foils as recently proposed.[11,33]

Thus, as presented in Scheme 1, this work aims to demonstrate the suitability of AWs generated in piezoelectric plates to induce ice-phobicity and provide ice detection. We trust that proving the effectiveness of the AWs de-icing concept in close-to-real scenarios should open the way for future industrialization and applications of evolved versions of systems based on this principle. In addition, it is expected that demonstrating the reliability of simple and non-expensive model AWs devices based on commercially available piezoelectric plates, extended electrodes, and these systems after their modification with anti-icing layers, will provide the ever-growing anti-icing scientific community with an approachable methodology to advance in the development of a new generation of industrially-oriented, energy-efficient and smart de-icing systems.

2. Results and Discussion

2.1. Simulation of AWs

We have recently shown that the excitation configuration proposed in Scheme 1 and Figures S1 and S2 (Supporting Information), consisting of two planar electrodes on LiNbO$_3$ plates subjected to rf signaling at ≈3.5 MHz, generates patterns of acoustic standing waves[34] with a submillimeter wavelength. Since the de-icing and active anti-icing processes studied in this work can be quite dependent on the AW characteristics, the generated standing AWs have been simulated using the procedure described in the experimental and method section.

As in the experiments, we found a narrow-banded drop in the return loss computed at each simulated frequency, indicating a strong coupling between the electric excitation and the AW mode at that frequency. The resonance frequency of this coupling was identified as 3.509 MHz (Figure S6, Sup-

porting Information), in good agreement with the experimental results. The deflection of the chip at resonance is presented in **Figure 1**a). Here snapshots during a period of a single vibration (T) are presented. An animation of a full cycle can be found in Video S1 (Supporting Information). Note, that the displacement of the surface is exaggerated (by a factor of 3000). The colors of the figure give a more realistic view of the vibration's magnitude, which was in the order of tens of nanometers (for 1 W excitation power). The most important finding is the large in-plane displacement, suggesting a shear-dominant AW mode. Figure 1b) presents the three displacement components along the centerline of the plate surface. We found that the shear component of the displacement was one order of magnitude larger than the normal component. Furthermore, the excited AW mode resulted to be the first thickness-shear mode of the plate with an acoustic standing wave in the direction of the plate thickness. The frequency of this resonance depends on the material properties and the thickness of the substrate, but barely on the other dimensions of the device. This was confirmed in the experiments, where chips with different surface areas and electrode dimensions (but identical thickness) had very similar resonant frequencies. The findings suggest that the normal displacement of the chip surface (observed numerically, but also experimentally, e.g., in vibrometer tests in ref. [34]) is a disturbance of the fundamental shear AW mode, rendered by the mechanical boundary conditions and the finite plate dimensions. It is noteworthy that the simulation only gives
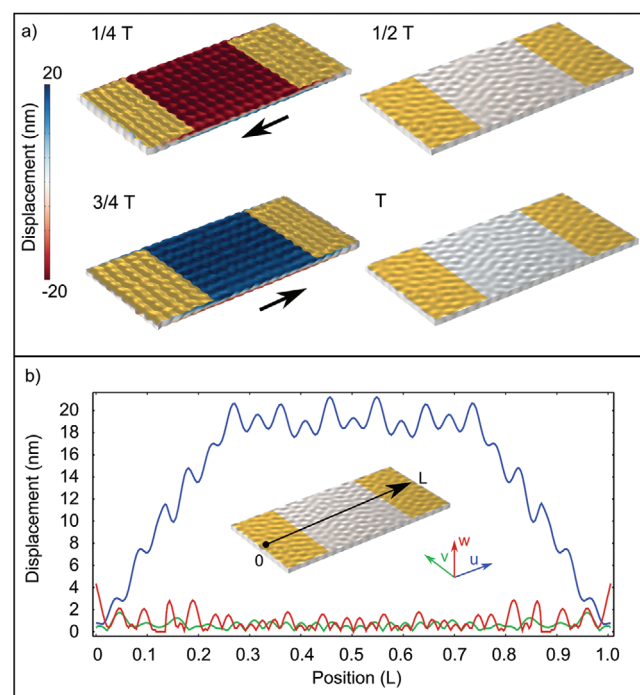
Figure 1. Vibration of the LiNbO$_3$ plate with planar electrodes, computed with the FE method at the designed frequency. a) Snapshots of the displacement fields (exaggerated with a scaling factor of 3000) at different fractions of a single period of the vibration (T). b) Absolute values of the displacement fields along the center-line, revealing a dominating share mode. An animation of the vibration is included in the supplementary material of the paper (Video S1, Supporting Information).

**ADVANCED
SCIENCE NEWS**

www.advancedsciencenews.com

**ADVANCED
FUNCTIONAL
MATERIALS**

www.afm-journal.de

a qualitative assessment, as the true boundary conditions are unascertainable from the conducted experiments.

In the next sections we will describe the observed effects of these AWs on specific icing experiments, which, carried out as explained in the experimental section, should be primarily considered as resulting from the shear excitation mode of the induced AW. It must be remarked that other AW modes might deliver slightly different effects and efficiency, although we expect that basic mechanisms should be equivalent to those reported here.

2.2. Melting and De-Icing of Ice Aggregates

The first step of this investigation consisted of determining the influence of various experimental variables on the melting of water and ice droplets upon AW activation of a piezoelectric substrate. We examined the following variables: a) effect of temperature on the resonant conditions of the plates; b) idem by dripping water onto the surface and the formation of ice aggregates upon cooling; c) effect of the AW excitation of the piezoelectric substrate inducing de-icing. Herein, we will address these issues considering three types of piezoelectric substrates: bare substrates with an intrinsic hydrophilic wetting behavior, surface modified substrates with a hydrophobic/anti-icing behavior, and black non-pyroelectric LiNbO₃. Previous to reporting the results of the studied icing processes, we describe selected properties of surface-modified LiNbO₃ chip plates.

2.2.1. Hydrophobically and Anti-Icing Treated LiNbO₃ Plates

To render the LiNbO₃ plate surface hydrophobic, we used ZnO thin films fabricated by PECVD and subsequently modified with a hydrophobic CFₓ layer or upon grafting with hydrophobic molecules. Although these ZnO thin films are relatively compact, their surface is known to present a certain roughness,[35,36,38] a feature that according to the Wenzel wetting model[45] will contribute to increasing the surface hydrophobicity and/or serve as a suitable anchoring layer of water repellent molecules. The basic characteristics of the films used in the present study are shown in **Figure 2**. Figure 2a,b) show normal and cross section micrographs of a ZnO film illustrating its microstructure and surface morphology. ZnO thin films prepared by PECVD were crystalline and depicted a preferential crystallographic orientation with the (101) planes parallel to the surface.[28] It is noteworthy that fluorination with the PFOTES molecules (see below) did not induce appreciable changes in the microstructure or crystallinity of the films. In addition, the inset in Figure 2b) confirms the high transparency of the ZnO thin films, a requirement for the future implementation of AW activation procedures onto transparent devices (e.g., for display or photovoltaic applications).

Surface functionalization consisted of the fabrication of a ZnO/CFₓ bilayer, or the grafting of PFOTES molecules to get a ZnO(F) layer (see Experimental Section). The grafting process used to prepare the ZnO(F) layer entails the reaction of the methoxy groups attached to the silicon atom of the grafting PFOTES molecule with –OH groups on the surface of the
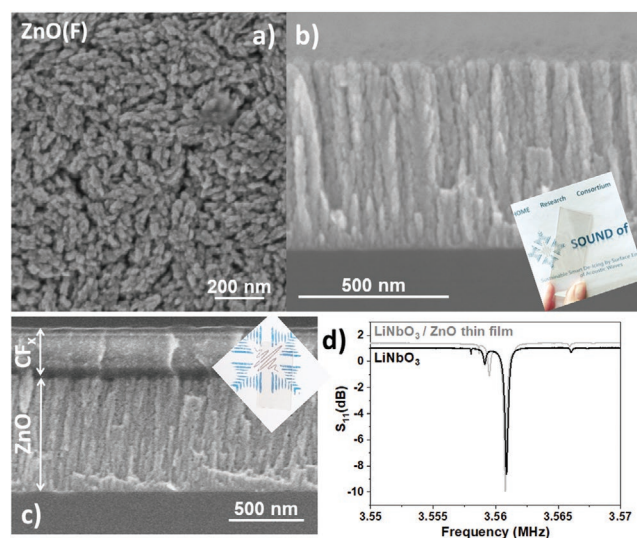

Figure 2. Thin film layers and multilayers fabricated by plasma-assisted methods as topcoats of bulk piezoelectric plates. SEM micrographs of the fluorinated ZnO a,b) and a CFₓ polymeric thin film on ZnO c). Insets in (b) and (c) demonstrate the high transparency of the layers and multilayers deposited on the piezoelectric plates. d) Comparison of the return loss spectra for the bare and modified LiNbO₃ plates as indicated in the plot.

oxide. In this regard, the higher surface roughness of the ZnO thin films with respect to the LiNbO₃ plates is favorable to enhance the grafting capacity of the outer surface of the devices and, therefore, to increase their hydrophobic and anti-icing capacity.[46] Figure 2c) shows a typical SEM cross-section view of a ZnO (800 nm)/CFₓ (300 nm) bilayer (see Figure S7, Supporting Information for the top-view SEM image). This cross section highlights the good definition and flat character of the interfaces existing between LiNbO₃ and ZnO, as well as between ZnO and CFₓ, where no large voids, imperfections, or defects can be devised. The planarity of interfaces is a requirement for a straightforward transmission of AWs through multilayer structures.[47,48] X-ray photoelectron spectroscopy analysis confirmed that the CFₓ films presented a PTFE-like composition where CFₓ chains with CF₃, CF₂, and CF functional groups constitute their basic structure[26,27] (see Figure S7, Supporting Information). In previous works, we have demonstrated that these films are hydrophobic, conformal to rough surfaces, and may induce a Cassie-Baxter wetting regime,[49] as well as a robust *passive* anti-icing response.[40,46,50,51]

Both the ZnO/CFₓ and ZnO(F) device terminations showed a hydrophobic behavior. The wetting contact angle at room temperature determined for a 5 µL water droplet placed onto the LiNbO₃+ZnO/CFₓ and LiNbO₃+ZnO(F) surfaces was 110° and 133° (within at least 5% of uncertainty), respectively, compared to 55° for the bare LiNbO₃ surfaces. Please consider, that according to the Young-Dupré equation[52] ($W_{SL} = \gamma_l(\cos\theta + 1)$, for a MilliQ water surface tension (γ_l) of 72.13 mN m⁻¹, the work of adhesion at the interface between the water drop and these surfaces would be 113.50 mN m⁻¹, 47.46 mN m⁻¹ and 22.94 mN m⁻¹ for LiNbO₃, LiNbO₃+ZnO/CFₓ, and LiNbO₃+ZnO(F), correspondingly. The sliding angle (i.e., the tilting angle of the plate required for the displacement of the

**ADVANCED
SCIENCE NEWS**

www.advancedsciencenews.com

**ADVANCED
FUNCTIONAL
MATERIALS**

www.afm-journal.de

drop on the surface) was higher than 90° in the two cases. These surface characteristics are expected to modify the interface interaction between substrate and water droplets during the freezing and melting processes.

Regarding the interaction of AWs and ice, a crucial issue is to verify that the electromechanical properties are not significantly affected by the functionalization coating, particularly because the non-ideal behavior of the polycrystalline films as compared with the crystalline character of the substrate plate might induce a certain AW attenuation (see next sections showing that, effectively, resonance frequency was quite sensitive to the environment, amount of water or ice, temperature, and similar parameters). To discard significant damping or alteration of the AWs upon device functionalization, return loss spectra were recorded for the bare $LiNbO_3$ plate and the same plate with a ZnO film deposited onto its surface. The corresponding spectra reported in Figure 2d) are practically identical (except for a small frequency shift that could be attributed to small differences in the fixing of the plates to the sample holder), thus sustaining that, from the point of view of AW activation, the plates remain practically unmodified after the deposition of the ZnO thin film. The same behavior was found for $LiNbO_3$-ZnO/CF_x and -ZnO(F) device chips.

2.2.2. $LiNbO_3$ Plate Resonance and Freezing of Water Droplets

A series of essays were first carried out to monitor the evolution of the plate resonant behavior through the typical steps of a water droplet freezing experiment,[29,40,53–55] namely: 1) dripping water directly on the surface of the piezoelectric substrate at a temperature > 0 °C, 2) progressive rapid cooling to the desired minus zero temperature and 3) verification of the freezing of the water droplet by optical observation.

It is noteworthy by this experimental sequence that step 3) may occur at temperatures well below zero (i.e., water remains in a super-cooled state) and take a considerable time due to various freezing delay factors.[56] **Figure 3** shows the evolution of the return loss spectra (S_{11}) recorded when varying the temperature for a series of $LiNbO_3$ plates without (i.e., dry) and with a 5 µL water droplet deposited onto their surface (Figure 3 a,b), respectively). According to this figure, the narrow shape of the S_{11} spectra of the AWs generated in the $LiNbO_3$ plate permits a very accurate determination of temperature or other phenomena affecting the piezoelectric vibrations. Such a precise dependence is not possible with SAWs, which are characterized by a much broader profile.[11] Figure 3a) shows the series of spectra recorded for the dry plate decreasing the temperature from 18 °C down to −20 °C. Figure 3c) shows that a linear shift in the position of the return loss minimum occurs with temperature. This dependence was completely reversible upon increasing the temperature and is characterized by a slope of −85 ppm °C^{-1}, in good agreement with reported values (−86.44 ppm °C^{-1}) of the temperature coefficient constant of $LiNbO_3$.[57–59] Figure 3b) also gathers an equivalent series of S_{11} spectra recorded for the same plate but with a 5 µL droplet deposited onto the surface and subjected to a freezing process. Despite the wider shape of the signal, attributable to the presence of the water droplet on the surface of the chip, the S_{11}
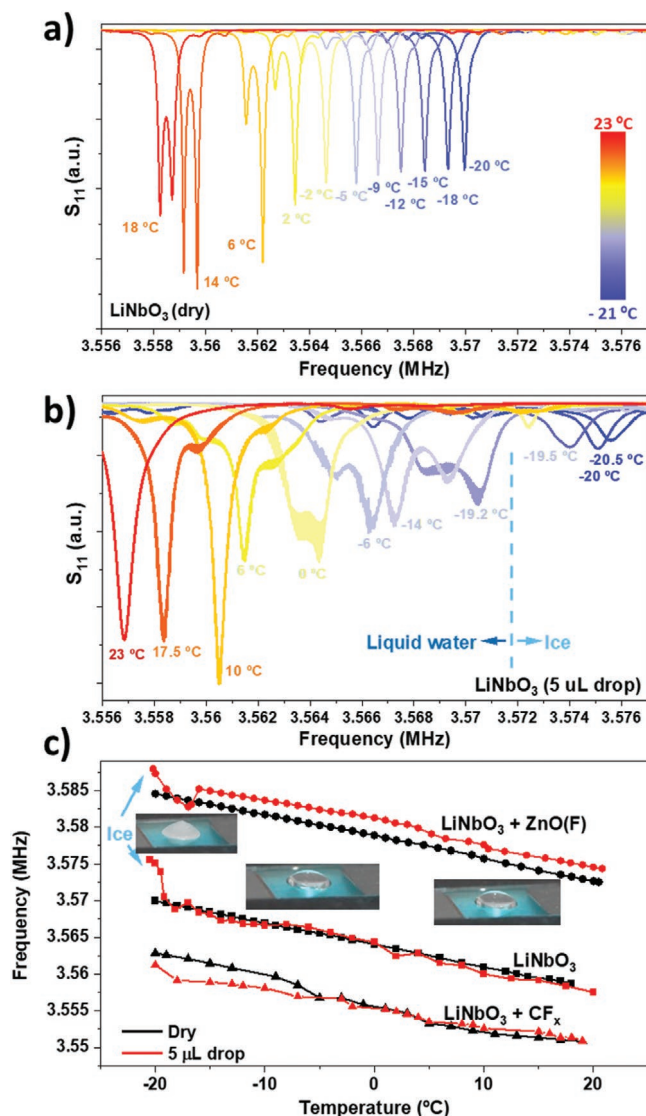

Figure 3. Variation of return loss spectra of bare and modified $LiNbO_3$ plates with planar electrodes as a function of temperature and in the presence of water droplets and ice aggregates. a) Return loss spectra (i.e., S_{11} coefficient) of the $LiNbO_3$ plate as a function of frequency for decreasing temperatures from 18 to −20 °C. b) Idem for this plate with a 5 µL water droplet on the surface. The drastic attenuation and shape change of the S_{11} spectrum after freezing respond to the transformation of water into ice. Please consider that the color bar is the same for a) and b). c) Plot of the frequency of S_{11} minimum against temperature for the bare and modified $LiNbO_3$ plate chips with and without water droplet (5 µL) on their surface. The arrows signal the points at which the super-cooled water droplet transforms into ice. The insets show photographs of a characteristic water droplet before and after its transformation into ice.

return loss signal experienced a similar frequency shift with temperature, provided that the water droplet remained liquid or in a supercooled state. As evidenced in Figure 3c), a drastic increase shift in resonance takes place upon water freezing. From a practical perspective, the similar linear variations irrespective of the presence of a water droplet on the surface suggest the possibility of extending the use of $LiNbO_3$, already utilized for high-temperature monitoring,[59,60] as a temperature

sensor under humid and low-temperature conditions. The capacity to detect icing processes and to monitor the water-ice conversion is an additional function implicit in Figure 3b), showing that freezing of deposited water not only induces a sharp increase in resonance frequency of the S_{11} signal but also changes in its shape and intensity. From a fundamental point of view, these changes at ≈ -20 °C, when the supercooled water droplet transforms into an ice aggregate, point to a drastic modification of the electromechanical properties of the device. Such a result agrees with recent evidence by Anisimkin et al.,[19] who monitoring the S_{12} parameter, have shown that a SAW LiNbO$_3$ plate ice sensor operated with IDTs presented a much higher attenuation coefficient in the presence of surface ice than with water.

It is important to stress that we found a similar linear evolution with temperature when comparing the results obtained with the bare LiNbO$_3$ substrate plate with those for this plate covered with an anti-icing coating, i.e., for samples LiNbO$_3$-ZnO(F), LiNbO$_3$-ZnO/CF$_x$ or LiNbO$_3$/CF$_x$ (Figure 3c). Similarities also exist with respect to the sharp increase in frequency accompanying the water-ice transformation (Figure 3c). This similar behavior indicates that the found variation with temperature responds solely to the effect of the temperature coefficient constant of LiNbO$_3$,[57,59] an effect agreeing with the predominant shear character of the AWs generated in the chip device utilized for the experiments. It is also noteworthy that the observed reproducible dependence of the S_{11} resonance with temperature was also found for black LiNbO$_3$ (see Figure S8,

Supporting Information), a feature supporting that the variation of electromechanical properties with temperature are equivalent for these two types of LiNbO$_3$ plate substrates.

2.2.3. Ice Melting with AW Activated LiNbO$_3$ Plates

The previous analysis of the variation of LiNbO$_3$ return loss spectra with temperature and the formation of ice on its surface has revealed a high dependence of the resonance frequency on these two experimental variables. It also indicates that an efficient ice removal via plate wave excitation of these substrates would require precise and continuous tuning of the resonance frequency during the de-icing process (see a detailed description of the tuning procedure in the Experimental Section).

Melting tests of ice aggregates were first carried out on a bare LiNbO$_3$ substrate. The time evolution of the ice aggregate profile upon AW activation determined from the side image of the droplet recorded with a photo camera is depicted in **Figure 4**a)-left. These profiles are compared with those observed during a de-icing test induced by slow natural warming up to ambient temperature, just by letting equilibrate the temperature of the substrate where experiments were carried out with that of the external medium (i.e., corresponding to a temperature variation rate of 0.02° s^{-1} as measured with a thermocouple emplaced at the substrate, the complete melting sequence can be followed in Video S2, Supporting Information). A first remarkable finding is the short time required to achieve complete

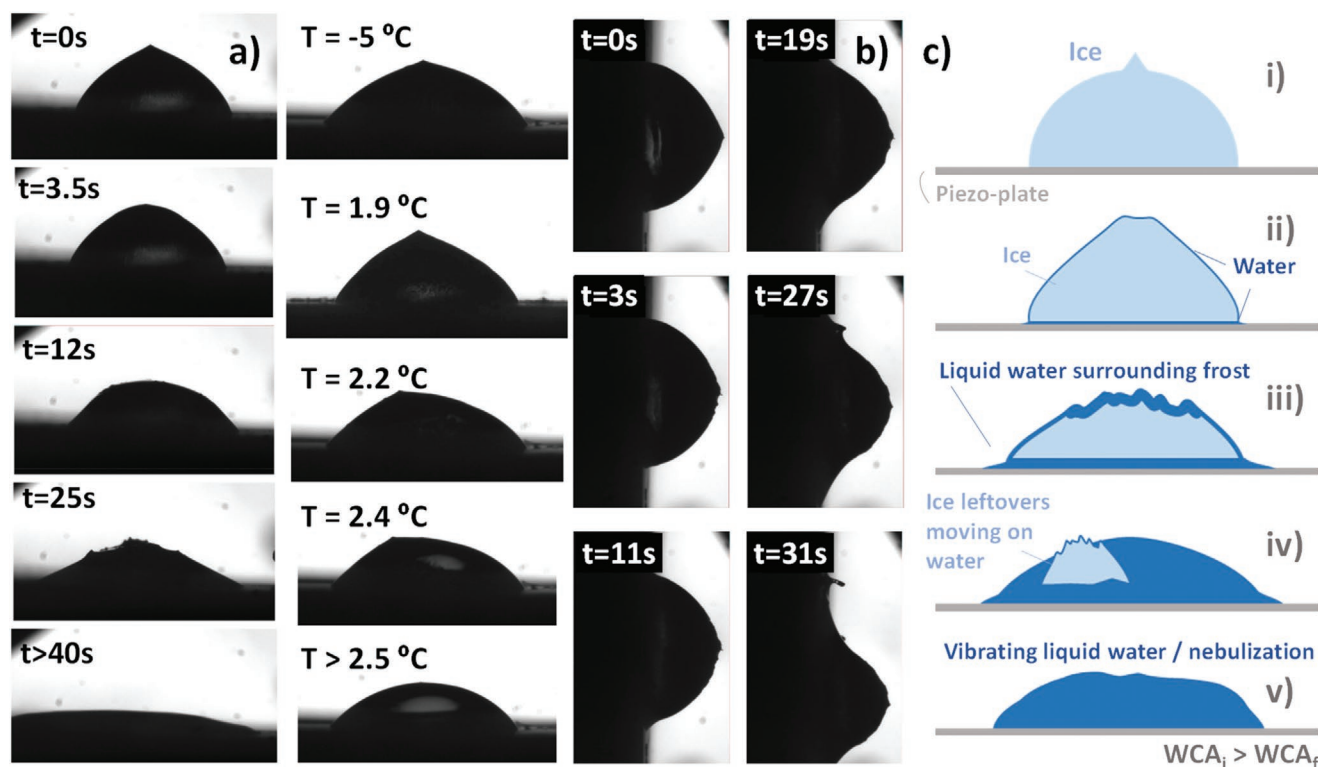**Figure 4.** Ice melting process mechanism through the analysis of profile snapshots of ice aggregates onto LiNbO$_3$ substrates. a) Comparison of ice melting process for an ice aggregate excited with AWs (left) and by natural warming up (right). b) Ice melting process induced by AWs for the substrate placed vertically. c) Cartoon representing the ice/water evolution during the AW-induced ice melting process.

**ADVANCED
SCIENCE NEWS**

www.advancedsciencenews.com

**ADVANCED
FUNCTIONAL
MATERIALS**

www.afm-journal.de

melting, 41 s, by the AW activation with a 40 V rf excitation signal. It is also noteworthy that the aggregate shape during the melting process induced by AWs differs substantially from the profile found when performing the melting by a natural warming up (Figure 4a-right). In particular, it appears that in intermediate (e.g., see snapshot at 25 s in Figure 4a-left) and final states (snapshot at 41 s) liquid water spreads onto the surface to a larger extension than for the warmed-up ice aggregate (e.g., the water droplet profile in Figure 4a-right after complete melting defines a wetting contact angle of ≈10°, against ≈30° for the droplet resulting from natural melting, the complete-time elapse in this case was ≈5 min 50 s as seen in Video S2, Supporting Information. The complex mechanism underlying this flattening effect, the so-called "acoustowetting", has been studied extensively in recent years, e.g. by Manor et al.[61–63] These results also suggest that during AW activation and partial melting, water forms and accumulates at the outer surface of the ice-drop, including also the ice-substrate interface and, upon progressive melting, spreads onto the entire drop volume and the substrate surface. The interface melting as an intermediate step in the AW de-icing mechanism agrees with a dominantly shear wave-driven melting mechanism and is further supported by the experiments in Figure 4b and Video S3 (Supporting Information). The former shows a series of photographs taken during an AW-induced de-icing experiment with the substrate and ice aggregate placed vertically. The series of snapshots presented in this figure reveals that at intermediate states of the de-icing process, the remaining ice spreads over the surface and tends to move outside the image frame. This spreading indicates a limited adhesion to the substrate, in agreement with the formation of a water interlayer and the action of the gravitational force. The cartoons in Figure 4c reproduce, in an ideal way, the observed evolution of the ice aggregate under AW activation for 41 sec. They represent a progressive melting of the ice aggregate at the interface, the spreading of water both onto the substrate and over the remaining core of ice (note that the water contact angle on ice is very small if not zero and can easily spread over its surface).[64,65] Regarding the efficiency of the AW transmission, those conditions where water and ice coexist on the surface would likely release the attenuation in the AW transmission found after the formation of ice (i.e., Figure 3b), provided that the substrate contacts an interlayer of liquid water and not directly ice. This effect stems from the high effectiveness of AWs to energize water, as widely studied for the AW propagation in water droplets.[66,67]

Interestingly, black LiNbO₃ behaves similar to the standard LiNbO₃ regarding the activation of the melting process of ice aggregates, as illustrated by the images provided in Figure S9 (Supporting Information). This sequence of images was taken along an experiment similar to that in Figure 4 and the results suggest that electromechanical activation processes rather than a pyroelectric effect are the main cause of the AW-induced melting of ice. This is an important distinction because it stresses that during the initial stages of ice activation, mechanical effects may induce cracking and other forms of energizing the ice interface and that only in a second stage, water heating and leaky waves, known to form in AW activated water droplets, will be the dominant factors of de-icing. We will thoroughly discuss such stages in an incoming report on glace ice melting by SAWs.

2.3. Ice Adhesion Tests

Ice adhesion strength on substrates is a fundamental interface property to achieve an efficient anti-icing response of solid surfaces.[33,41,50,68] Within a holistic approach, both surface chemistry and roughness should affect ice adhesion. Regarding the latter, it is usually admitted that the rougher the surface the higher the ice adhesion force between ice agglomerates and substrates.[69] The experiments gathered in this section aim at determining the effects of AW interaction on ice adhesion. It is noteworthy to stress that experiments are carried out in tensile mode, which permits minimizing the affectation of results by the likely dynamic variations of adhesion due to partial melting at the ice substrate interface.

Essays have been carried out with the bare (and therefore sub-nm flat) LiNbO₃, perfluoro molecule-functionalized LiNbO₃ (LiNbO₃(F)) and the LiNbO₃ covered with anti-icing coatings (i.e., LiNbO₃ + ZnO(F) and LiNbO₃ + ZnO/CF$_x$). Such modifications convert the piezoelectric plate surface into hydrophobic but, as discussed in the previous sections, at the expense of incorporating a certain surface roughness, particularly in the case of ZnO coating. Ice adhesion experiments on the different devices were carried out following the experimental protocol described in the experimental section, either without or with AW activation, and using a vertical pulling-off tensile configuration. RF amplitude voltages of 20 and in the range 35/40 V were applied to the chip electrodes while pulling with an increasing force until the complete detachment of the ice probe. These AW excitation conditions did not induce the ice melting in the cantilever, although a limited interface melting or softening should be expected. It is also noteworthy that the application of a pulling force to the ice probe adhered to the surface may modify the resonance conditions of the piezoelectric device, e.g. by mechanical deformation of the substrate. This is evidenced in **Figure 5**a comparing S₁₁ spectra taken while applying either a zero or a net pulling force of 1 N. Experiments were carried out at the same temperature to ensure that chip resonance variation was only related to the pulling action and not to the dependence on temperature (cf. Figure 3). The shift in resonance frequency highlights the high sensitivity of the system to the environmental conditions and the need to finely tune the frequency of the applied AW excitation signal while performing the ice adhesion tests (note that a systematic analysis of return loss spectra as a function of the pulling force might be used to derive pressure sensing information with these devices).[41] This adjustment was systematically done before performing the actual adhesion tests under AW activation. Characteristic force/time curves recorded during ice adhesion test experiments are shown in Figure 5b for sample LiNbO₃+ZnO(F) while applying a voltage of 0 V (i.e., passive conditions) or 35 V. The two curves are characterized by the progressive increase in the pulling force with time resulting from a progressive upward movement of the dynamometer that pulls off the ice probe. This continuous increase is suddenly stopped when the ice probe becomes detached from the surface. The maximum recorded value corresponds to the force required to detach the probe and can be used to estimate the adhesion strength under each working condition. The first result of the experiments was that the force required to detach the probe was significantly smaller when
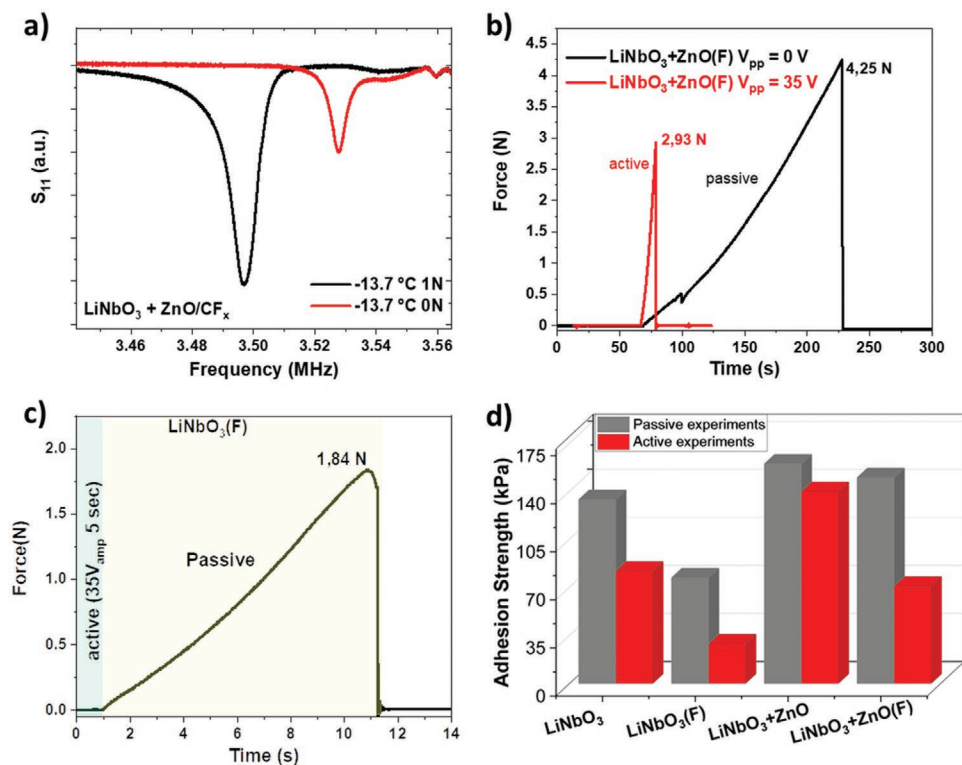
Figure 5. Ice adhesion behavior under AW activation. a) Return loss spectra for a LiNbO$_3$+ZnO/CF$_x$ chip with the ice probe stuck on its surface without applying a force and while applying a pulling force of 1 N at the same temperature. b) Force–time curves recorded with the dynamometer for sample LiNbO$_3$/ZnO(F) without activation (reference experiment) and while applying a constant voltage of 35 V (i.e., under AW activation). c) Idem for sample LiNbO$_3$(F) combining AW activation and pulling sequentially: first the piezo plate was activated at the resonance frequency (35 V) for 5 s, then the pulling was carried out with increasing force until ice detachment. d) Comparison of ice-adhesion strengths for the LiNbO$_3$ and modified LiNbO$_3$ chip plate samples. "Passive" essays were carried out on the same chip surfaces without applying the AW activation.

AWs were generated in the substrate during the detachment experiment (see values of adhesion strength in Figure 5d). In a recently published ice adhesion study using a shear-actuated device under AW activation, authors observed a decrease in ice adhesion attributed to an increase of dipole spacing at the interface provoked by the nanoscale surface vibration of the piezoelectric.[33] In addition to this or similar interface effect, the pull-off experiments carried out here evidence that the interface softening induced by the AW activation favors the complete detachment of the ice and its separation from the surface in a sharp way, which minimizes possible interferences due to interface water layers.

The hypothesis of a certain interface softening or modification of the ice probe, although not directly accessible with the pull-off procedure, is supported by the experiment in Figure 5c addressing the combination of active and passive working conditions. In this experiment, the rf excitation (at 35 V) was applied to the LiNbO$_3$(F) chip for 5 sec without applying any force. Immediately after, pulling started and induced detachment at an extremely low force value of 1.84 N (i.e., adhesion strength 20 kPa). Such a result indicates that the ice adhesion is significantly reduced during the very first seconds of AW excitation, which must produce an effective softening of the ice interface with the piezoelectric plate. Although the exact nature of this softening process at the ice-substrate interface should be a question of debate to be addressed in future investigations,

we wonder whether an initial ice cracking and partial melting induced at the ice interface during the first 5 sec of AW activation is responsible for this behavior. In this regard, it is noteworthy that the pull-off plot in Figure 5c does not end in a sharp termination, but in a rounded curve, suggesting that the ice-substrate interface is not homogeneous in this case.

We should note that, for practical applications, this working mode might reduce the energy consumption for the AW detachment of ice in real scenarios where ice removal could be induced upon application of sequential pulses and be even driven by self-deicing mechanisms, i.e., ice falling by its weight, splitting into debris, or detached by neighboring droplets.[70]

As a summary of the experiments, Figure 5d gathers the adhesion strength values determined from the Force–time curves for a series of experiments carried out with LiNbO$_3$, LiNbO$_3$(F), LiNbO$_3$-ZnO, and LiNbO$_3$-ZnO(F) under AW actuation and pulling off. Values for reference experiments without AW activation are included for comparison. A first look at the reference samples (i.e., "passive" experiments) indicates that, in good agreement with the literature,[25,50,68,71] the hydrophobic character and the roughness are critical characteristics determining the adhesion strength. Thus, the adhesion strength is smaller for the hydrophobic LiNbO$_3$(F) sample than for the bare LiNbO$_3$ substrate, while the rougher LiNbO$_3$+ZnO(F) and LiNbO$_3$+ZnO samples present the highest adhesion strengths of the whole series. It is noteworthy that this trend is opposite

to what is expected in the case of the interface between liquid water and the surface (c.f. W_{SL} values estimated above). On the other hand, much lower values of adhesion strengths were obtained while activating the substrates with AWs. Thus, most values reported in Figure 5d are smaller than 100 kPa, a value usually taken as the threshold for low-adhesion substrates. In some cases, values ≈20 kPa were obtained, which are deemed characteristics of extremely low adherent surfaces.[70] Moreover, data in this figure show that the higher the applied voltage, the lower the adhesion strength. In good agreement with the essays carried out on non-activated (passive) samples, for the activated systems, hydrophobicity contributes to reducing the adhesion strength of ice (perfluorinated surfaces present lower adhesion values), while roughness (i.e., ZnO coated) increases it.

In summary, the set of adhesion strengths reported in Figure 5 confirms that the AW activation of piezoelectric substrates decreases the ice adhesion, contributing to an easier removal detachment of ice from surfaces.

2.4. De-Icing and Active Anti-Icing in an IWT

In this section, we check whether the AW activation of chip substrates contributes to decreasing their ice accretion capacity, as well as promoting the de-icing of already accreted ice. Both sets of experiments were carried out under conditions close to those in real scenarios. For this purpose, we placed the plate holder with the chip plates in an IWT operated under the conditions described in the experimental section (see also Figure S5, Supporting Information) and three air velocities: 25, 50, and 70 m s^{-1}. Previous to de-icing and ice accretion experiments, the response of the piezoelectric plate was monitored as a function of wind tunnel velocity. **Figure 6**a shows the return loss spectra obtained for a bare LiNbO$_3$ plate placed in the wind tunnel exposed at −6 °C to dry air flows at the three velocities selected for the experiments. It is apparent that the resonance peak broadens and becomes displaced a few tenths of kHz when exposing the plate to increasingly higher air velocities. Although a detailed analysis of the factors contributing to this systematic variation is outside the scope of the present work (e.g., pressure drops due to Bernoulli effects or local tempera-

ture fluctuations might be involved in these variations), these findings further support the possibilities and high sensitivity of LiNbO$_3$ plates for environmental monitoring.

Similar to freezing experiments reported in Figure 3, changes in the return loss spectra during the icing process were also monitored in the IWT. An example of the icing monitoring capacity of the device is reported in the Figure S10 (Supporting Information), showing the return loss spectra recorded in static conditions of the IWT (i.e., in the absence of wind) at −6 and −6.5 °C for a LiNbO$_3$ plate with a supercooled water droplet on its surface and the ice aggregate resulting from the droplet freezing, respectively. Return loss spectrum after freezing in the IWT depicted a considerable decrease in intensity, a widening, and a clear shift in the frequency of resonance maximum. From the perspective of the AW activation of the devices in the IWT under operating conditions (i.e., a mixture of supercooled water droplets in an air flow), the observed shift of the resonance frequency with the wind speed (Figure 6a) and the water-ice transformation (Figure S7, Supporting Information) makes it compulsory to tune the resonance peak before and during the icing experiments. This strategy, explained in the experimental section, was systematically applied during the realization of the experiments reported next.

2.4.1. Active Anti-Icing in IWT

The first set of results deals with the active anti-icing capacity (ice accretion prevention) of the AW-activated piezoelectric plates. Figure 6b shows an image taken in the IWT after an ice accretion test on the AW-activated bare piezoelectric plate (applied voltage 30 V) and a reference LiNbO$_3$ plate. We should note that, for a better comparison, the selected voltage for this experiment is the same as for the de-icing experiment described next. Nevertheless, it does not imply that an effective active anti-icing effect could not be achieved at lower voltages. The image taken after 9 min shows that a big amount of ice becomes accreted on the reference plate, but no ice appears on the AW-activated chip. A detailed evolution of the accumulation of ice on the reference substrate and the occasional formation of small droplets of water on the activated substrate during this
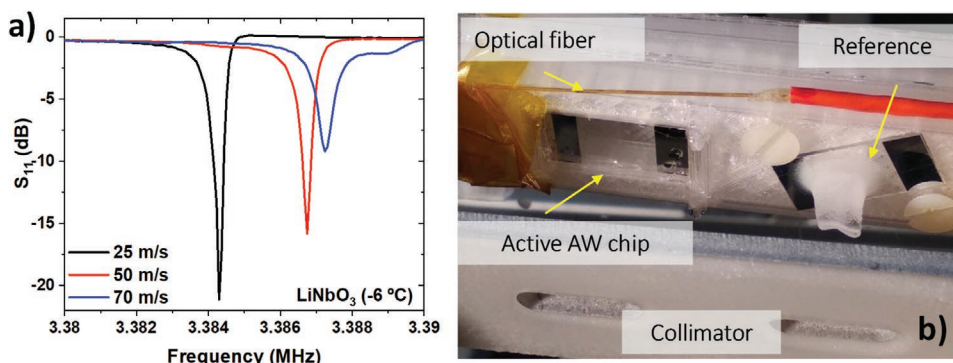

Figure 6. Results of active anti-icing test in an IWT. a) Return loss spectra recorded for a LiNbO$_3$ plate at −6 °C in dry conditions under the action of different wind speeds as indicated. b) Photograph of the sample holder emplaced in the IWT behind the collimator after conducting an active anti-icing experiment where a high amount of glace ice became accreted on the reference sample. The AW-activated chip remained ice-free. Main elements of the experiment appear labeled in the photograph.
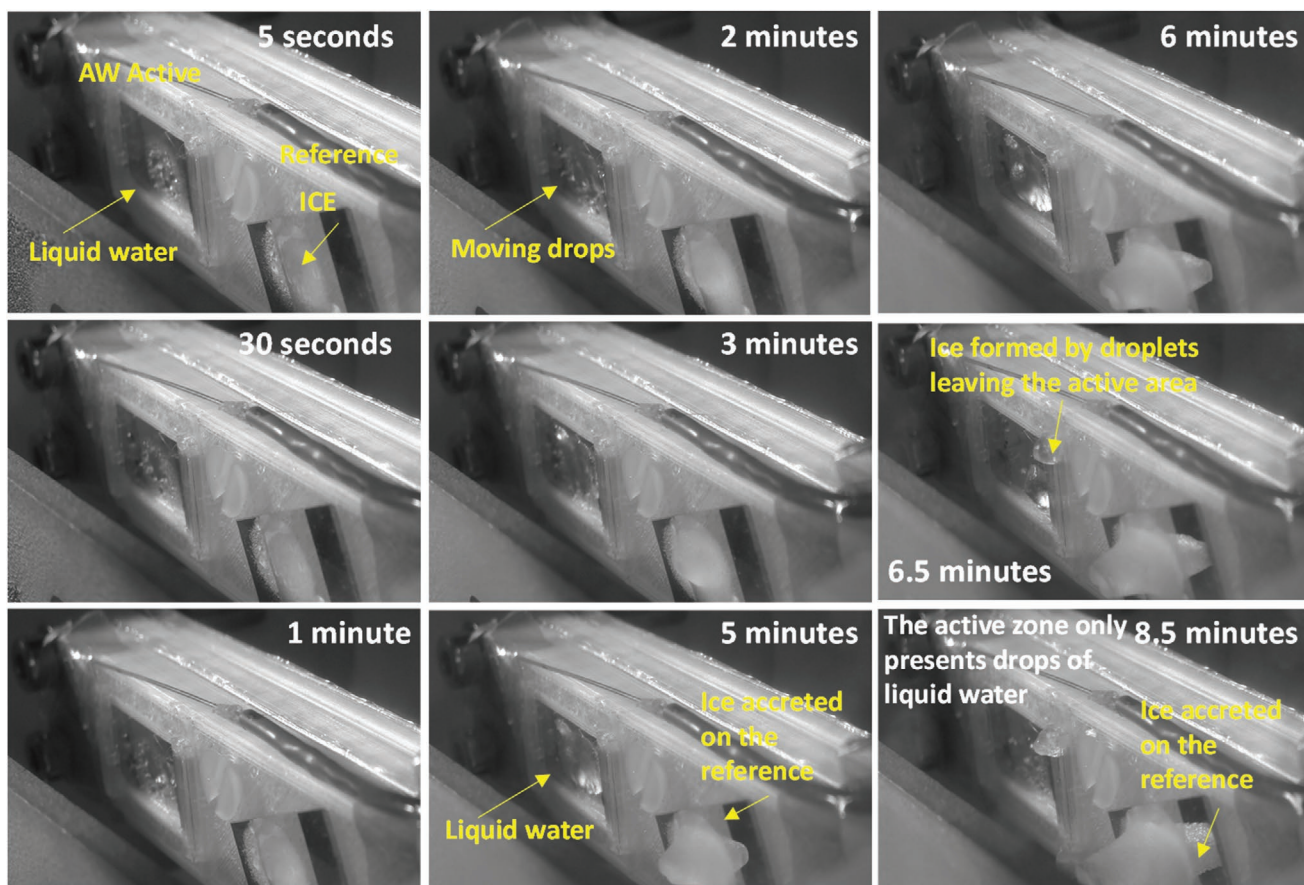
Figure 7. Characteristic active anti-icing experiment carried out in the IWT under realistic conditions. Successive snapshots from an ice accretion experiment revealing the active anti-icing capacity of the AW to prevent the formation of ice aggregates onto the surface of a bare LiNbO$_3$ plate. The left and right sides of the pictures correspond to the AW activated and reference sample, correspondently. Maximum amplitude 30 V. IWT conditions: Glaze ice, $v = 25$ m s^{-1}, SAT $= -8$ °C; LWC $= 0.5$ g m^{-3}, MVD $= 20$ μm.

experiment can be seen in the snapshots provided in **Figure 7** and Video S4 (Supporting Information). It is noteworthy that during this experiment the temperature was continuously monitored by an optical fiber sensor placed beside the piezoelectric plate (Figure 6b) and by a thermographic camera and that their maximum readings (for the fiber sensor) and the camera colors corresponding to the hottest zones were achieved during AW activation of the plate. The found effectiveness of the AW activation to avoid ice formation must be the consequence of various factors such as the low adhesion of ice on the AW-activated substrates (see Figure 5d)) and their capacity to prevent the freezing of the large amount of small droplets of water (Figure 4). The remarkable final effect is that no ice became accreted on the activated substrate, while the area on the reference substrate that was sustained by the slit entrance of the shield (see Figure S5, Supporting Information) was covered by a thick layer of glace ice.

According to Video S4 (Supporting Information), the monitoring of temperature with the optical fiber showed a maximum increase up to −3 °C (keeping temperature below zero for the entire experiment), while the thermocamera color variations suggested a slight increase in temperature over the area of inspection. It is noteworthy in Video S4 (Supporting

Information) that the higher temperatures detected by the thermocamera correspond to the areas beneath the metal electrodes (i.e., away from the chip central location where ice is to be formed), which appear already glowing during the tunning of the resonance frequency. This evidence further sustains that Joule heating of metal electrodes plays a minimum role in the anti-icing activation of the chips.

2.4.2. De-Icing in IWT

In the absence of AW activation ice became equally accreted on the reference sample and the device chip. De-icing experiments could then be carried out under the working conditions of the IWT (i.e., under the direct effect of supercooled water droplets impinging on the substrate at the set wind velocities) and with an equivalent layer thickness of ice both on the reference and the AW activated chips. The series of snapshots in **Figure 8** and Video S5 (Supporting Information) show that ice could be effectively melted and removed by the airflow from the surface of the LiNbO$_3$ chip plate when activating the piezoelectric with AWs. This particular experiment was carried out after ice formation, applying 30 V input voltage and the IWT operated at
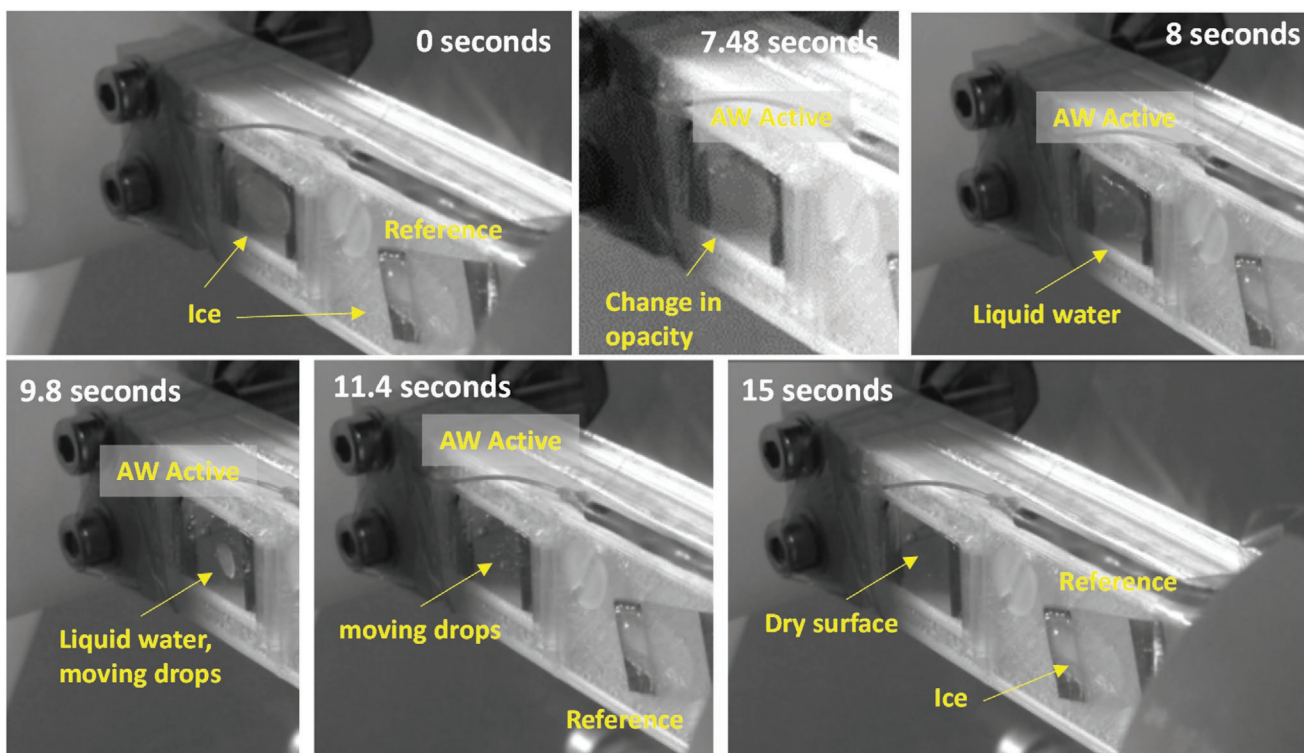
**ADVANCED
SCIENCE NEWS**

www.advancedsciencenews.com

**ADVANCED
FUNCTIONAL
MATERIALS**

www.afm-journal.de

Figure 8. Characteristic de-icing experiment carried out in the IWT under close to real conditions. Successive snapshots from an ice accretion experiment showing the fast de-icing by AWs of the ice covering the LiNbO$_3$ chip plate. Maximum amplitude 30 V. IWT conditions: Glaze ice, $v = 70$ m s^{-1}, SAT $= -8$ °C; LWC $= 0.5$ g m^{-3}, MVD $= 20$ um)

a wind velocity of $v = 70$ m s^{-1} at a temperature of −8 °C and bearing supercooled water droplets as explained in the experimental section. Remarkably, ice remained unaltered on the reference sample, but on the AW activated sample ice first changed opacity just after 7.5 s of applying the AWs and became molten after 8 s. The resulting water droplets were dragged out from the surface of the AW activated piezoelectric plate, which appeared completely dry just after 15 s since the beginning of the activation process. For the experiments in Figure 8, the optical fiber sensor measured a maximum temperature of −5 °C just at the moment of ice melting: the synchronized Video S5 (Supporting Information) reports such an instant showing a sudden increase of a few degrees in the monitoring of both the optical fiber reading and the thermocamera colors.

Both de-icing and active anti-icing experiments described above were carried out with bare LiNbO$_3$ plates, as well as for the surface modified substrates LiNbO$_3$+ZnO(F) and LiNbO$_3$+ZnO/CF$_x$. **Figure 9** gathers the applied voltages required to achieve equivalent de-icing and active anti-icing effectiveness for various samples and wind velocities from 0 to 70 m s^{-1}. In all cases, the optical fiber sensor renders values similar to those provided during the experiments reported in Figures 6–8. The purpose of these experiments was to determine the minimum voltage required in each case although, as discussed below, uncertainties in this regard exist for the active anti-icing experiments and consequently the comparison must be done carefully. Thus, the series of voltage values in Figure 9 can be used only as an indicative parameter of the efficiency
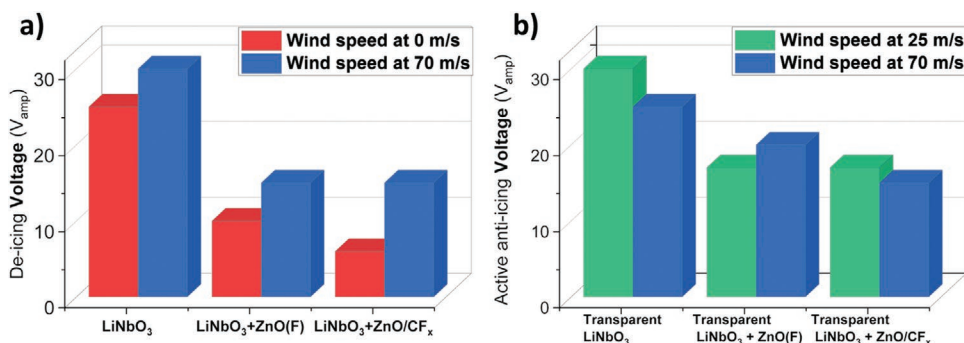

Figure 9. Summary of required voltages for selected de-icing a) and active anti-icing b) experiments in the IWT facility.

of the respective process under investigation and conclusions should be taken as qualitative because some parameters cannot be precisely determined under the IWT working conditions (e.g., the actual volume of accreted ice for de-icing experiments or amount of ice accreted on the reference sample for the active anti-icing tests). With these restrictions, the series of voltage values gathered in the figure indicate that the surface-modified substrates, characterized by a hydrophobic behavior, required less power than the bare substrates for equivalent de-icing or active anti-icing results. It can be also realized that, in de-icing experiments, the required power increased for higher wind velocities. Such a neat tendency is not straightforwardly deduced in the active anti-icing experiments, where higher voltages were generally required at high wind velocity, though with the discrepancy of $LiNbO_3+ZnO(F)$ samples. However, we must stress that these slight differences in voltage can be within the error bar of the experiments since, under these conditions, visual difficulties to identify the (absence) of accretion processes inside the IWT may lead to applied voltage values higher in a few volts than the minimum threshold values required to prevent icing. Therefore, the most relevant evidence from Figure 9a,b is that the needed voltage required to, respectively de-icing and active anti-icing, is smaller for hydrophobic than bare chip substrates.

These pieces of evidence taken under close to real environmental conditions confirm the positive effect of hydrophobicity on the AW de-icing and active anti-icing. For de-icing, high wind velocities decrease the efficiency likely indicating that some heat produced in the system is more easily released under the action of a high-speed wind. Such a feature still requires further analysis considering factors such as actual pressure at the position of the plates and the actual value of water vapor pressure in contact with the accreted ice, this latter a variable that is known to contribute to the efficiency of de-icing under well-controlled Joule laboratory conditions[72] (since water vapor pressure in teh air flow should be defined by its equilibrium with the supercooled droplets of water, it is likely that at high wind velocities vapor pressure drastically decreases at the chip substrate location where ice forms). Although durability tests of the anti-icing properties of the proposed coatings under realistic conditions are far from the scope of this article, it is worth mentioning that the surface properties of the tested samples were durable after multiple ice-adhesion experiments and icing/de-icing cycles. Previously reported results on the durability of the anti-icing properties of these coatings[29,40] further support such a claim. In addition, Table S1 (Supporting Information) compares the initial WCA of the ZnO/CF_x and the value of this paramter measured just after activation of the acoustic waves and 24 h later. The found slight variation in the recorded values is in good agreement with the above-mentioned[62] acoustowetting effect encountered a few seconds after the activation of the surface and with an incipient recovery of the initial values after storage.

3. Conclusion

In this article, we have investigated a series of fundamental effects involved in the de-icing, active anti-icing, ice-monitoring and related ice removal processes induced by AW excitation of piezoelectric plates. Experiments have been performed with a model piezoelectric system consisting of $LiNbO_3$ single crystal plates where standing acoustic plate waves with a majority shear character are generated by rf activation of two extended metal electrodes. This model material system has revealed itself ideal to afford the study of a series of key issues of great relevance for icing and has provided first-hand evidence on the following key findings:

i) It has been demonstrated that the functionalization of $LiNbO_3$ plate with a ZnO(F) thin film or a ZnO/CF_x multilayer renders the substrate surface hydrophobic while leaving unaffected its AW excitation capacity.

ii) Results have proved the influence of the wetting behavior and surface roughness of the (modified) plates on phenomena such as ice melting, ice adhesion or ice accretion. In general, surface hydrophobicity favors the anti-icing character of the piezoelectric chip devices, reducing the AW power required to induce de-icing or prevent icing (active anti-icing).

iii) The comparison between standard (transparent and non-pyroelectric) and pyroelectric (black) $LiNbO_3$ has served to discard that, to a first approximation, pyroelectric activity plays a significant role in the AW de-icing processes, thus supporting the hypothesis of mechano-acoustic mechanisms for the initial stages of ice melting by AWs.

iv) The same piezoelectric plate devices have been demonstrated to be useful to analyze de-icing processes at laboratory scale (i.e., for small ice aggregates), as well as close to real conditions in an icing wind tunnel (i.e., for thick layers of glace ice). Mechanisms and procedures could be straightforwardly extrapolated, and conclusions regarding ice adhesion, accretion, de-icing and active anti-icing have gained a common ground for analysis and modeling.

v) Recording the return loss spectra of the AWs generated in the plate devices has revealed a high accuracy in the monitoring of parameters such as temperature or pressure and, in the case of icing, to detect freezing and melting processes. It is proposed that this capacity sets the basis for future developments combining sensing and smart actuation with the same device.

The sustaining analysis enabling these conclusions has been carried out with AWs with a predominant shear character. Whether this is a critical characteristic of the AWs when used for de-icing, is a question to be disclosed in the future with experiments where the AWs have a predominant out-of-plane component.

4. Experimental Section

Piezoelectric Plate Actuator and Experiment Design: The piezoelectric substrates utilized in the experiments consisted of double-side polished, single-crystalline $LiNbO_3$ plates (128° Y-cut, ca. 0.5 mm thickness, 1×2 cm^2 or 1.5×3 cm^2 size, Roditi International Corporation Ld.). "Black" $LiNbO_3$ plates (Hangzhou FreqControl Electronic Technology) of the same size and crystal orientation cut were also used for dedicated experiments.

Radiofrequency (rf) electrical signals were applied onto two metal contacts 0.5 or 1 cm in width and 1 or 1.5 cm in length consisting of a Ti/Al bilayer of 5 / 295 nm thickness prepared by the lift-off technique

and electron beam evaporation. Alternatively, contacts were also made by Ag layer electrodes (300 nm) prepared by DC-sputtering or simply by soft pressing a metal (Ta or Cu) foil (0.35 mm thickness, dimensions 0.5/1 cm) of the same dimensions located at the same position that the thin film contacts. No significant differences in AW actuation were found when comparing results obtained with these different types of electrodes.

To carry out the different active anti-icing/de-icing experiments, the plates working as chips were placed in a specifically designed and custom-built sample holder, which is presented in detail in the Supporting Information section, see Schematic 1 and Figure S1 (Supporting Information). A previous version of such a holder was developed by the authors to study the growth of TiO_2 thin films prepared by magnetron sputtering under acoustic wave activation.[34] In that work, we proved that Lamb-type standing AWs are generated with this electrode-plate configuration. A characteristic feature of the holder system is that the piezoelectric plate is held just by two soft metal spring bolts (1 mm diameter with the conical tip pressed onto the metal electrodes), and two holdings points or a thin bar at the lateral edges of the plate, respectively. This configuration ensures that attenuation of the plate oscillations by the polymeric frame is minimized (see Figure S1, Supporting Information). The electrodes are placed at the back of the plate, and thereby not exposed to the external icing environment, a significant difference in comparison with recent papers using SAWs and IDTs, where metallic electrodes are exposed to ice.[11,33] A reference sample (i.e., not subjected to AW activation) can be placed very close to the active piezoelectric plates for a proper evaluation of icing results, as discussed in the next section. This comparative analysis is deemed essential to undoubtedly differentiate the icing effects induced by the AWs.

AW activation was carried out as indicated in the Supporting Information section Figure S2 (Supporting Information). The electrical system utilized for AW excitation of the piezoelectric substrates consisted of an rf signal generator (Agilent 8648A Synthesized RF generator, Keysight technologies), a high power amplifier ZHL-5 W (Mini-Circuits), a vector network analyzer (VNA) (SDR-Kits, VNA 3SE), an oscilloscope (Siglent SDS 1204X-E), and a switching device to connect the piezoelectric substrate either to the VNA or the rf signal source. The signal could be continuously varied in voltage amplitude (up to 50 V, with a minimum set at 10 V) and in frequency (≈3.4–3.5 MHz, a value around which it appears the resonance frequency mode of the plates used for the experiments). The precision allowed by the RF generator was 0.0001 MHz. Used values of voltage and frequency are indicated for each experiment. Under such experimental conditions, a standing Lamb wave excitation mode of AWs can be generated on the piezoelectric plate as already mentioned[34] and will be simulated in the present work (see below). The two electrodes on the piezoelectric plate were respectively connected to the rf signal source (i.e., function generator plus amplifier) and ground, in this latter case, intercalating a resistor to determine the $I(t)$ curves. $V(t)$ and $I(t)$ curves were continuously recorded with the oscilloscope connected as indicated in Figure S2 (Supporting Information).

A typical experimental protocol to control the generator signal consisted of the following steps:

1. Acquisition of the return loss spectrum (i.e., S_{11} parameter) of a chip as a function of driving frequency. A typical example taken for a bare $LiNbO_3$ substrate chip is shown in Figure S3 (Supporting Information). It can be realized in this figure that each plate is characterized by a single or various narrow resonance peaks in the 3.4–3.6 MHz range. For the experiments, the function generator is set at the frequency of the highest minimum of the return loss spectrum (in the example of Figure S3 of Supporting Information, at 3.5609 MHz).

2. Application of the rf excitation signal at the set frequency and follow-up the icing/de-icing event of interest.

3. Dynamic re-adjustment of the rf excitation frequency at the S_{11} minimum after the change of acoustic load, e.g. due to freezing or droplet aerosolization. Determination of changes in the S_{11} minima was done by intermittent switching between VNA and the signal source.

Simulation of Generated AWs: A numerical study was carried out to further understand the complex vibration patterns at the plate resonance. A $LiNbO_3$ plate with electrodes (without holder and circuit board) was modelled using a predefined set of 3D coupled electrodynamic and mechanic equations in the commercial finite element (FE) solver COMSOL Multiphysics version 6.0 (similar to the numerical setup described in ref. [34]). The geometry of the plate had the same dimensions as the devices used in the experiments. The bulk material was described with an anisotropic, linear-elastic, and piezoelectric material model, using the stiffness, piezoelectric, and permittivity tensors for transparent $LiNbO_3$ depicted in ref. [35]. Preliminary computations at the design frequency did not show a noticeable effect of the mass and stiffness of the aluminium electrodes on the observed vibrations (not shown). Therefore, the electrodes were simplified as 2D, massless, and soft patches at the surface of the bulk material. The plate was discretized with a rectilinear grid with first-order shaped elements, consisting of 40 650 nodes, resulting in 928 144 degrees of freedom. Computations at the design frequency with different mesh densities showed the independence of the results from the resolution of discretization (not shown). The mechanical boundary conditions mimicked the mounting of the device during the experiment, as in Figure S1 (Supporting Information), prohibiting displacements normal to the substrate surface at the connector pins and the outer chip surface opposing the electrodes. The electrical boundary conditions prescribed time-harmonic electric potentials uniformly distributed on the electrode patches. The frequency of the time-harmonic signal was varied from 3.4 to 3.7 MHz in 1 kHz steps, and the model was solved for each of the steps.

Surface Modification with Anti-Icing Grafting and Multilayers: Icing tests were carried out either using the bare $LiNbO_3$ substrates or these substrates functionalized by the deposition of various thin layers modifying the wetting and passive anti-icing response of the examined chip samples. Compared with a recent article in the literature claiming the modification of the piezoelectric surface with grafted molecules endowing hydrophobicity,[1] the approach here consists of the deposition of a layer or a multilayer coating on top of the piezoelectric plate with a twofold aim. On the one hand, to verify the synergistic effect of hydrophobicity to facilitate de-icing. On the other hand, and more critical to the final exploitation of this approach, to prove that AWs propagate through these upper layers maintaining the effective interaction mechanism with ice. The following surface terminations had been considered for this study:

Surface Modification with Anti-Icing Grafting and Multilayers—ZnO Thin Films: Polycrystalline ZnO thin films were deposited by plasma enhanced chemical vapor deposition (PECVD) at room temperature in an ERC MW plasma reactor as detailed elsewhere.[36–38] Typical thicknesses of the ZnO thin films deposited onto the $LiNbO_3$ substrate varied between 500 and 1500 nm, a range for which no significant differences were found by the de-icing and active anti-icing experiments.

Surface Modification with Anti-Icing Grafting and Multilayers—CFx, Teflon like Thin Films: CF_x thin films have been prepared at ambient temperature by PECVD in an rf parallel plate reactor. Full details of the preparation procedure of these thin films have been reported elsewhere.[26,27] CF_x thin films with thicknesses in the range of 100 to 200 nm were deposited directly onto the $LiNbO_3$ plates or onto ZnO coated plates. Hereafter, this bilayer arrangement will be named ZnO/CF_x.

Surface Modification with Anti-Icing Grafting and Multilayers—PFOTES Molecular Grafting: The bare or ZnO-coated $LiNbO_3$ plates were functionalized by the grafting of perfluorooctyltriethoxysilane (PFOTES) molecules following the procedure detailed in refs. [29,39]. The grafted ZnO layer will be labelled as ZnO(F) and the bare substrate as $LiNbO_3$(F).

It is noteworthy at this point that these coatings have been already tested for passive anti-icing applications and demonstrated high durability and cyclability upon successive icing experiments (e.g., more than six complete cycles for grafted structures [29] and five freezing/thaw cycles for the CF_x coatings).[40] High stability could be also verified in the present work after AW de-icing and active anti-icing experiments.

The morphology of these thin films was characterized by Scanning Electron Microscopy (SEM) in an S4800 FESEM microscope by Hitachi, working at 2 kV and a typical working distance between 2 and 3 mm.

The chemical state of the functionalization films had been determined by X-ray photoelectron spectroscopy (XPS) in a SPECS PHOIBOS-100 spectrometer operated with Al Kα radiation as the excitation source and 20 eV constant pass energy.

Icing Tests: Specially designed experiments had been carried out to get information about the effect of AW activation on the following icing issues and interactions: i) droplet icing and melting; ii) ice adhesion; iii) ice accretion, under the premises of de-icing and active anti-icing processes, as described in the following:

Icing Tests—Droplet Icing and Melting: These experiments encompassed the deposition of water droplets directly onto the piezoelectric substrate, their freezing upon cooling, and their subsequent melting by AW activation. The analysis had been carried out either in a cooling chamber or on a Peltier plate emplaced in the controlled temperature chamber of an OCA20 goniometer (Dataphysics). The temperature was decreased from ambient temperature to values between −5 and −20 °C. Enlarged images of the water droplets, taken with a high-resolution photo camera in cross section view, have been analyzed to disclose the basic mechanism of melting while activating the substrate with AWs. In parallel, the S_{11} parameter is recorded with the VNA as a function of temperature and when the melting events are taking place. It will be shown that these spectra provide accurate information on the actual temperature of the piezoelectric plates, as well as on the freezing/melting processes of the water droplets.

Icing Tests—Ice Adhesion Tests: Ice adhesion tests were carried out by the pull-off method described in detail elsewhere.[41] Instead of the shear way of applying the force in most common ice adhesion tests,[33] herein a tensile mode was applied to produce ice detachment. The purpose of these experiments was to show differences between AW-activated and not activated substrates and the effect of hydrophobic coatings. Please consider that this mode minimizes any dynamic effect or variation in adhesion when a water interlayer forms between ice and substrate. As it will be shown by the reported results, the tensile detachment of the ice probe was rather sharp and, provided that all experimental conditions were maintained fixed, permits a straightforward comparison as a function of the AW intensity and surface characteristics (i.e., hydrophobicity). The experimental setup and detailed description of the pulling probe attached to the piezoelectric device ready for activation are reported in the Figure S4 (Supporting Information). The experiment proceeded by emplacing a hollow Teflon cylinder on the sample surface and filling it with 1 mL of Milli-Q water (cylinder's internal diameter is 9.86 ± 0.12 mm, its area 76.4 ± 1.9 mm², and the water level was ≈13 mm). Then, the sample was placed in a freezing chamber and left to freeze at a temperature of −10 °C, waiting until full solidification is reached. Once the ice was formed, a pulling force was applied through a thread connected to a dynamometer (IMADA ZTA-200N/20N), which, placed outside the cooling chamber, was attached to a motorized linear stage (IMADA MH2-500N-FA). The thread was subjected to a progressively increasing force until the ice probe became released from the surface. The applied force was perpendicular to the sample (tensile mode of analysis) and was continuously read by the dynamometer. It can be directly converted into adhesion strength values by referring the value of the force producing the detachment of ice to the area of the probe, (i.e., Force(N)/Area(m²), magnitude expressed in stress units of MPa). The setup was adapted to make it compatible with AW de-icing conditions. Different experiments were carried out under passive conditions (i.e., without applying the rf signal to the chip), continuous rf actuation of the chip for a defined voltage, and the combination of both (i.e., activating the chip for a given time and then applying the force without rf activation).

Icing Tests—Ice Accretion, De-Icing, and Active Anti-Icing in IWT: Ice accretion experiments were carried out to test the de-icing and active anti-icing performance of piezoelectric substrates under AW activation. Tests were carried out in an IWT facility located at INTA (Madrid, Spain) and described elsewhere.[29,41,42] Experiments were done using liquid water contents (LWC) in the range 0.18 – 0.22 g m⁻³, supercooled droplets with 20 µm of median volume diameter (MVD) in size distribution, a temperature from −5.5 to −8.5 °C, and three wind tunnel speeds: 25,

50, and 70 m s⁻¹ (i.e., within a subsonic regime where spurious heating effects could be discarded). De-icing and active anti-icing experiments in IWT have been usually carried out to test conventional Joule effect heating,[43] but to the best of knowledge, this has been the first time that these experiments are applied to test de-icing by acoustic waves. The lack of references and standards for this type of experiment brings about some uncertainties when dealing with data on a quantitative basis, a situation that requires dedicated research work already ongoing by the authors. Therefore, the analysis herein must be taken as qualitative and would be focused on determining differences when comparing results on the bare or coated (hydrophobic) LiNbO₃ substrates. Ice accretion was monitored simultaneously on AW-activated LiNbO₃ substrates and the reference non-actuated surface placed beside. To control the arrival direction of the air and water flow onto the plates, a screen frame with two slits of 67 mm² was placed before them at a distance of 19 mm. The geometry of this screen setup and related experimental details are presented in Figure S5 (Supporting Information). The evolution of the ice accretion on the surface of the reference and AW-activated piezoelectric plates was followed by direct video imaging of their surfaces. The evolution of temperature at the surface of the AW-activated chip plate during the experiments was monitored with a Testo 890 thermographic camera and, close to the chip, with a Fiber Bragg Grating Sensor (FBGS®). The optical fiber polyimide coating of this sensor was previously removed to avoid decalibration and replaced with a polyimide isolation capillary. The measurements were done using a LUNA Si155 Interrogator. The optical fiber was calibrated using SIKA TP3M165E2 highly precise temperature calibrator and a cubic calibration curve.[44]

Supporting Information

Supporting Information is available from the Wiley Online Library or from the author.

Acknowledgements

Conflict of Interest

The authors declare no conflict of interest.

Data Availability Statement

The data that support the findings of this study are available from the corresponding author upon reasonable request.;

Keywords

[1] V. G. Grishaev, I. S. Borodulin, I. A. Usachev, A. Amirfazli, V. P. Drachev, N. I. Rudenko, R. K. Gattarov, I. K. Bakulin, M. V. Makarov, I. S. Akhatov, *Int. Commun. Heat Mass Transf.* **2021**, *129*, 105698.

[2] M. Pourbagian, W. G. Habashi, *Int. J. Heat Fluid Flow* **2015**, *54*, 167.

[3] L. Li, S. Khodakarami, X. Yan, K. Fazle Rabbi, A. A. Gunay, A. Stillwell, N. Miljkovic, *Adv. Funct. Mater.* **2022**, *32*, 2201521.

[4] X. Yin, Y. Zhang, D. Wang, Z. Liu, Y. Liu, X. Pei, B. Yu, F. Zhou, *Adv. Funct. Mater.* **2015**, *25*, 4237.

[5] H. Zhang, X. Xu, M. Wu, Y. Zhao, F. Sun, Q. Xin, Y. Zhou, M. Qin, Y. Zhou, C. Ding, J. Li, *Adv. Funct. Mater.* **2022**, *32*, 2201795.

[6] Y. Li, W. Ma, Y. S. Kwon, W. Li, S. Yao, B. Huang, *Adv. Funct. Mater.* **2022**, *32*, 2113297.

[7] X. Meng, H. Hu, C. Li, A. A. Abbasi, J. Cai, H. Hu, *Phys. Fluids* **2019**, *31*, 037103.

[8] N. Li, Y. Zhang, H. Zhi, J. Tang, Y. Shao, L. Yang, T. Sun, H. Liu, G. Xue, *Chem. Eng. J.* **2022**, *429*, 132183.

[9] H. Habibi, L. Cheng, H. Zheng, V. Kappatos, C. Selcuk, T.-H. Gan, *Renew. Energy* **2015**, *83*, 859.

[10] V. Daniliuk, Y. Xu, R. Liu, T. He, X. Wang, *Renew. Energy* **2020**, *145*, 2005.

[11] D. Yang, R. Tao, X. Hou, H. Torun, G. McHale, J. Martin, Y. Fu, *Adv. Mater. Interfaces* **2021**, *8*, 2001776.

[12] J. L. Rose, *Ultrasonic Guided Waves in Solid Media*, Cambridge University Press, Cambridge **2014**.

[13] X. Ding, P. Li, S.-C. S. Lin, Z. S. Stratton, N. Nama, F. Guo, D. Slotcavage, X. Mao, J. Shi, F. Costanzo, T. J. Huang, *Lab Chip* **2013**, *13*, 3626.

[14] F. Hadj-Larbi, R. Serhane, *Sens. Actuators Phys.* **2019**, *292*, 169.

[15] Y. Q. Fu, J. K. Luo, N. T. Nguyen, A. J. Walton, A. J. Flewitt, X. T. Zu, Y. Li, G. McHale, A. Matthews, E. Iborra, H. Du, W. I. Milne, *Prog. Mater. Sci.* **2017**, *89*, 31.

[16] S. V. Venna, Y.-J. Lin, G. Botura, *J. Aircr.* **2012**, *44*, 509.

[17] Y. Yin, L. Cheng, W. Wang, Y. Zhang, Y. Liang, *AIP Adv.* **2021**, *11*, 115028.

[18] M. Pohl, Proceedings Int. Workshop on Atmospheric Icing of Structures, IWAS 2022, Mc Gill Univeristy, Montreal, Canada, June 19–23.

[19] V. Anisimkin, V. Kolesov, A. Kuznetsova, E. Shamsutdinova, I. Kuznetsova, *Sensors* **2021**, *21*, 919.

[20] H. Cho, M. Hasanian, S. Shan, C. J. Lissenden, *NDT E Int* **2019**, *102*, 35.

[21] Y. Liu, K. Fu, J. Liu, Y. Tian, H. Zhang, R. Wang, B. Zhang, H. Zhang, F. Zhou, Q. Zhang, *Appl. Surf. Sci.* **2019**, *497*, 143663.

[22] P. Guo, Y. Zheng, M. Wen, C. Song, Y. Lin, L. Jiang, *Adv. Mater.* **2012**, *24*, 2642.

[23] W. Li, Y. Zhan, S. Yu, *Prog. Org. Coat.* **2021**, *152*, 106117.

[24] Y. Q. Fu, J. K. Luo, X. Y. Du, A. J. Flewitt, Y. Li, G. H. Markx, A. J. Walton, W. I. Milne, *Sens. Actuators, B* **2010**, *143*, 606.

[25] M. I. Jamil, A. Ali, F. Haq, Q. Zhang, X. Zhan, F. Chen, *Langmuir* **2018**, *34*, 15425.

[26] A. Terriza, R. Álvarez, A. Borrás, J. Cotrino, F. Yubero, A. R. González-Elipe, *J. Colloid Interface Sci.* **2012**, *376*, 274.

[27] A. Terriza, M. Macías-Montero, M. C. López-Santos, F. Yubero, J. Cotrino, A. R. González-Elipe, *Plasma Process. Polym.* **2014**, *11*, 289.

[28] X. Wu, Z. Chen, *J. Mater. Chem. A* **2018**, *6*, 16043.

[29] V. Rico, J. Mora, P. García, A. Agüero, A. Borrás, A. R. González-Elipe, C. López-Santos, *Appl. Mater. Today* **2020**, *21*, 100815.

[30] Y.-Q. Fu, H.-F. Pang, H. Torun, R. Tao, G. McHale, J. Reboud, K. Tao, J. Zhou, J. Luo, D. Gibson, J. Luo, P. Hu, *Lab Chip* **2021**, *21*, 254.

[31] H. Jin, J. Zhou, X. He, W. Wang, H. Guo, S. Dong, D. Wang, Y. Xu, J. Geng, J. K. Luo, W. I. Milne, *Sci. Rep.* **2013**, *3*, 2140.

[32] A. V. Yatsenko, S. V. Yevdokimov, A. S. Pritulenko, D. Y. Sugak, I. M. Solskii, *Phys. Solid State* **2012**, *54*, 2231.

[33] X. Zeng, Z. Yan, Y. Lu, Y. Fu, X. Lv, W. Yuan, Y. He, *Langmuir* **2021**, *37*, 11851.

[34] A. García-Valenzuela, A. Fakhfouri, M. Oliva-Ramírez, V. Rico-Gavira, T. C. Rojas, R. Alvarez, S. B. Menzel, A. Palmero, A. Winkler, A. R. González-Elipe, *Mater. Horiz.* **2021**, *8*, 515.

[35] G. Kovacs, M. Anhorn, H. E. Engan, G. Visintini, C. C. W. Ruppel, *IEEE Symp Ultrason.* **1990**, *1*, 435.

[36] P. Romero-Gómez, J. Toudert, J. R. Sánchez-Valencia, A. Borrás, A. Barranco, A. R. Gonzalez-Elipe, *J. Phys. Chem. C* **2010**, *114*, 20932.

[37] X. García-Casas, A. Ghaffarinejad, F. J. Aparicio, J. Castillo-Seoane, C. López-Santos, J. P. Espinós, J. Cotrino, J. R. Sánchez-Valencia, Á. Barranco, A. Borrás, *Nano Energy* **2022**, *91*, 106673.

[38] J. Budagosky, X. García-Casas, J. R. Sánchez-Valencia, Á. Barranco, A. Borrás, *Plasma Process. Polym.* **2022**, *19*, e2100179.

[39] V. M.-W. Yim, A. S.-W. Lo, B. J. Deka, J. Guo, J. A. Kharraz, I. T. Horváth, A. K. An, *Green Chem.* **2020**, *22*, 3283.

[40] V. J. Rico, C. López-Santos, M. Villagrá, J. P. Espinós, G. F. de la Fuente, L. A. Angurel, A. Borrás, A. R. González-Elipe, *Langmuir* **2019**, *35*, 6483.

[41] P. F. Ibáñez-Ibáñez, F. J. Montes Ruiz-Cabello, M. A. Cabrerizo-Vílchez, M. A. Rodríguez-Valverde, *J. Colloid Interface Sci.* **2022**, *608*, 792.

[42] J. Mora, P. García, R. Muelas, A. Agüero, *Coatings* **2020**, *10*, 290.

[43] Z. Martin, T. Blanco, A. Butragueno, J. Sánchez, P. Vázquez, A. Scidà, V. Palermo, E. Treossi, F. Valorosi, *Rev. Mater. Compuestos* **2022**, *3*, 42.

[44] T. Ringel, T. Bosselmann, in *Proc. Sens. 2017*, AMA Service GmbH, Wunstorf, Germany **2017**, pp. 267–270.

[45] R. N. Wenzel, *J. Phys. Colloid Chem.* **1949**, *53*, 1466.

[46] A. J. Meuler, J. D. Smith, K. K. Varanasi, J. M. Mabry, G. H. McKinley, R. E. Cohen, *ACS Appl. Mater. Interfaces* **2010**, *2*, 3100.

[47] L. Y. Yeo, J. R. Friend, *Biomicrofluidics* **2009**, *3*, 012002.

[48] J. Reboud, Y. Bourquin, R. Wilson, G. S. Pall, M. Jiwaji, A. R. Pitt, A. Graham, A. P. Waters, J. M. Cooper, *Proc. Natl. Acad. Sci* **2012**, *109*, 15162.

[49] A. B. D. Cassie, S. Baxter, *Trans. Faraday Soc* **1944**, *40*, 546.

[50] A. J. Meuler, J. D. Smith, K. K. Varanasi, J. M. Mabry, G. H. McKinley, R. E. Cohen, *ACS Appl. Mater. Interfaces* **2010**, *2*, 3100.

[51] K. Golovin, S. P. R. Kobaku, D. H. Lee, E. T. DiLoreto, J. M. Mabry, A. Tuteja, *Sci. Adv.* **2016**, *2*, e1501496.

[52] R. Tadmor, R. Das, S. Gulec, J. Liu, H. E. N'guessan, M. Shah, P. S. Wasnik, S. B. Yadav, *Langmuir* **2017**, *33*, 3594.

[53] S. Jung, M. K. Tiwari, N. V. Doan, D. Poulikakos, *Nat. Commun.* **2012**, *3*, 615.

[54] G. Heydari, M. Sedighi Moghaddam, M. Tuominen, M. Fielden, J. Haapanen, J. M. Mäkelä, P. M. Claesson, *J. Colloid Interface Sci.* **2016**, *468*, 21.

[55] G. Heydari, E. Thormann, M. Järn, E. Tyrode, P. M. Claesson, *J. Phys. Chem. C* **2013**, *117*, 21752.

[56] F. J. Montes Ruiz-Cabello, S. Bermúdez-Romero, P. F. Ibáñez-Ibáñez, M. A. Cabrerizo-Vílchez, M. A. Rodríguez-Valverde, *Appl. Surf. Sci.* **2021**, *537*, 147964.

[57] J. Streque, T. Aubert, N. Kokanyan, F. Bartoli, A. Taguett, V. Polewczyk, E. Kokanyan, S. Hage-Ali, P. Boulet, O. Elmazria, *IEEE Sens. Lett.* **2019**, *3*, 9900134.

[58] M. R. H. Sarker, J. L. Silva, M. Castañeda, B. Wilburn, Y. Lin, N. Love, *J. Intell. Mater. Syst. Struct.* **2018**, *29*, 938.

[59] C. Zhao, W. Geng, X. Qiao, F. Xue, J. He, G. Xue, Y. Liu, H. Wei, K. Bi, Y. Li, M. Xun, X. Chou, *Sens. Actuators Phys.* **2022**, *333*, 113230.

[60] V. I. Anisimkin, N. V. Voronova, *Ultrasonics* **2021**, *116*, 106496.

[61] A. R. Rezk, O. Manor, J. R. Friend, L. Y. Yeo, *Nat. Commun.* **2012**, *3*, 1167.

[62] G. Altshuler, O. Manor, *Phys. Fluids* **2015**, *27*, 102103.

[63] O. Manor, M. Dentry, J. R. Friend, L. Y. Yeo, *Soft Matter* **2011**, *7*, 7976.

[64] C. A. Knight, *J. Colloid Interface Sci.* **1967**, *25*, 280.

[65] C. A. Knight, *Philos. Mag. J. Theor. Exp. Appl. Phys.* **1971**, *23*, 153.

[66] S. P. Zhang, J. Lata, C. Chen, J. Mai, F. Guo, Z. Tian, L. Ren, Z. Mao, P.-H. Huang, P. Li, S. Yang, T. J. Huang, *Nat. Commun.* **2018**, *9*, 2928.

[67] A. Salari, S. Appak-Baskoy, M. Ezzo, B. Hinz, M. C. Kolios, S. S. H. Tsai, *Small* **2020**, *16*, 1903788.

[68] V. Vercillo, S. Tonnicchia, J.-M. Romano, A. García-Girón, A. I. Aguilar-Morales, S. Alamri, S. S. Dimov, T. Kunze, A. F. Lasagni, E. Bonaccurso, *Adv. Funct. Mater.* **2020**, *30*, 1910268.

[69] Y. Zhuo, S. Xiao, A. Amirfazli, J. He, Z. Zhang, *Chem. Eng. J.* **2021**, *405*, 127088.

[70] P. Jin, X. Yan, M. J. Hoque, K. F. Rabbi, S. Sett, J. Ma, J. Li, X. Fang, J. Carpenter, S. Cai, W. Tao, N. Miljkovic, *Cell Rep. Phys. Sci.* **2022**, *3*, 100894.

[71] S. S. Latthe, R. S. Sutar, A. K. Bhosale, S. Nagappan, C.-S. Ha, K. K. Sadasivuni, S. Liu, R. Xing, *Prog. Org. Coat.* **2019**, *137*, 105373.

[72] K. Al-Khalil, T. Ferguson, D. Phillips, K. Al-Khalil, T. Ferguson, D. Phillips, in *35th Aerosp. Sci. Meet. Exhib.*, American Institute of Aeronautics And Astronautics, Inc., Reno, USA, 6–9 January **1997**.

2209421 (16 of 16)